Stretch-flanging of AA2024-T3 sheet by single-stage SPIF

J.A. López-Fernández, Gabriel Centeno*, A.J. Martínez-Donaire, D. Morales-Palma, C. Vallellano

Department of Mechanical and Manufacturing Engineering, University of Seville, Camino de los Descubrimientos s/n 41092, Sevilla (Spain)
*Corresponding author, Telephone number: +34 954 48 59 65, email: gaceba@us.es

Abstract: Flanging is a forming process that is commonly used in many high technology industrial applications such as the manufacturing of thin-walled aircraft structures as wing ribs that are formed using rubber-pad forming during the last forming stages with the aim of increasing the stiffness of the component edges. In addition, the performance of hole-flanged parts manufactured using incremental sheet forming (ISF) processes has been recently addressed, focusing especially in evaluating the formability enhancement, as well as the onset of failure utilising a variety of forming strategies. However, the process outputs for the manufacturing of other kind of flanges (i.e. straight, shrink or stretch flanges) have not been analysed so intensively yet. In this context, this work presents an experimental analysis of formability and failure within the forming limit diagram (FLD) of stretch flanges of AA2024-T3 performed by single point incremental forming (SPIF) for a wide range of process parameters. Furthermore, the numerical modelling of the stretch flanging process in combination with a theoretical framework based on Barlat's anisotropy plasticity criterion, allowed to assess the formability of the material within the triaxiality space, permitting to understand the stress/strain states attained in SPIF and the forming conditions upon which the onset of failure occurs.

Keywords: Single point incremental forming (SPIF); Stretch-flanging; Formability; Failure; Numerical modelling, Barlat's plasticity; Stress triaxiality.

1. Introduction

After the actual origin of incremental sheet forming (ISF) technologies in the late 70's (Mason, 1978) of last century, as suggested in the historical review by Emmens and Van den Boogaard (2010), and their later strong development from the 90's especially in Japan, including the first attempts for evaluating the forming limits in ISF (Iseki et al., 1994) and showing the main process applications for the production of shell components contending sharp corners (Kitazawa et al., 1994), a huge number of research work focused in ISF processes has been appearing during the last decades. These research activities have been compiled in an important number of review papers concentrating in essential topics of incremental sheet forming technologies such as the enhancement of formability (Emmens and Van den Boogaard, 2009), the influence of process parameters in the process outputs (Gatea et al., 2016), the current process progress and trends (Behera et al., 2017) as well as their prospects for the near future (Duflou et al., 2017).

Incremental sheet forming processes present a series of advantages in the sense of flexibility, rapid prototyping as well as economic manufacturing due to the suppression of expensive dedicated dies and equipment. Indeed, single point incremental forming (SPIF), the simplest alternative among ISF technologies, consists basically in a hemi-spherical tool guided by a CNC machine that follows a pre-establish trajectory for progressively forming a peripherally clamped blank into a final sheet component without the use of any dedicated die. In this regard, as exposed in Silva et al (2011), the most attractive benefit of SPIF/ISF technologies is their ability for increasing the sheet material formability up to the fracture forming limit (FFL), thus permitting to attain stable plastic deformation well above the forming limit curve (FLC). A number of

systematic studies have been carried out with the aim of evaluating this formability enhancement for metallic sheet material, including aluminium alloys as in Silva et al. (2014) or steels as in the work by Centeno et al. (2014), but also for polymeric materials (Bagudanch et al., 2017), as discussed in the review paper by McAnulty et al. (2017).

Despite the fact that the ISF technologies have not an important industrial implantation so far, its single point variant has been utilized for the manufacturing of a variety of sheet prototypes and final components. For example, research has been focused for the last few years on the production of hole-flanges by SPIF, as in Cui and Gao (2010) by means of evaluating the process capabilities for different types of tool strategies. Later, Centeno et al. (2012) provided a new level of understanding of multi-stage hole-flanging by SPIF combining circle grid strain (CGA) analysis with the independent characterization of the material forming limits. To this regard, the authors have recently analysed the single-stage SPIF variant (Borrego et al., 2016) that allows reducing the production time, one of the main disadvantages of ISF. In this regard, and only after the very preliminary research by Powell and Andrew (1992) in the early 90's focusing in the assessment of the forming forces, the paper of Voswinckel et al. (2013), enhanced in Voswinckel et al. (2015), was pioneer in studying the applicability of the SPIF process for obtaining convex (shrink) and concave (stretch) open flange geometries. These works analysed for the first time ever the limits of shrink and stretch flanging using SPIF by evaluating the capability of incremental forming for enhancing the formability in flanging or "flangeability".

In this sense, formability and failure in incremental forming have been usually analysed in the light of strain analysis within the principal strain space. Some works such as Silva

et al. (2010) by the beginning of this decade demonstrated that the limiting strains in SPIF coincided with the fracture limit. In addition, Soeiro et al. (2014) discussed how this fracture limit corresponds to mode I (in-plane tension) of fracture mechanics, providing an analytical framework to the stress/strain states attained in SPIF based on the membrane stress analysis by Martins et al (2010). Other authors such as Allwood and Shoulder (2009), in consonance with the work within the same research group of Jackson and Allwood (2009), pointed out the importance of shear stresses in incremental forming, which may become crucial as the sheet thickness increases. In this regard, Isik et al. (2014) provided an integrated vision of the fracture loci in sheet metal forming distinguishing the strain states leading to fracture in mode I of fracture mechanics (corresponding to plane tension) defined by the FFL, decreasing with a theoretical slope of "-1" from uniaxial towards equi-biaxial strain, and the fracture limit in mode II (in plane shear) defined by the Shear Fracture Forming Limit (SFFL), increasing in the second quadrant of the principal strain space from pure compression towards uniaxial strain with a theoretical slope of "+1". Nevertheless, some recent work by the authors such as Centeno et al (2017) pointed out that in the case of SPIF of conical testing parts, corresponding *a priori* to near plane strain, the fracture strains were slightly above the FFL obtained independently by means of Nakazima tests.

On the one hand side, the work of Martins et al (2014) suggested that in the case of sheet metal deformed by ISF, fracture in mode I is attained when the corresponding damaged function D reach a critical value D_c. The proposed damaged function expressed in Eq. 1 was the one suggested by Atkins (1996) by means of the level of accumulated stress triaxiality ratio, which is defined as the hydrostatic stress divided by the equivalent stress ($g = \sigma_m/\sigma_{eq}$). This equation is based on the damage criterion by

McClintock (1968) and it assumes that the accumulation of damage is principally due to void growth, neglecting the importance of void initiation and coalescence in incremental sheet forming.

$$D = \int_0^{\varepsilon_{eq}} g \cdot d\varepsilon_{eq} = \int_0^{\varepsilon_{eq}} \left(\frac{\sigma_m}{\sigma_{eq}}\right) d\varepsilon_{eq} \quad (1)$$

On the other hand side, the analysis of forming processes within the triaxiality space has revealed to be a significant tool for assessing material formability and failure. This analysis is based on the pioneer work by the Vujovic and Shavaik (1986) in the late 80's, later generalised by the work of Prof. Wierzbicki and collaborators, especially in Bao and Wierzbicki (2004) and later in Wierzbicki et al. (2005), resulting in what is informally called "Wierzbicki diagram" in the metal forming community. Indeed, in the triaxiality space, the different stress/strain states during the forming process are represented by the equivalent strain versus the stress triaxiality ratio. In this regard, Mirnia and Shamsari (2017) proposed a methodology for the prediction of failure in SPIF based in the utilization of the average triaxiality (defined in Eq. 2) for establishing an equivalent path within the triaxiality space valid both for proportional and especially for non-proportional loading paths, which is the case in incremental forming processes. More recently, the authors have analysed in Martínez-Donaire et al. (2019) the loading paths attained in hole-flanging by SPIF, explaining the high levels of principal strains at failure accomplished in this process, and thus demonstrating that the representation of these equivalent loading paths within the triaxiality space versus the corresponding forming limits of the material is of great importance for the accurate assessment of fracture in SPIF.

$$\bar{\eta} = \frac{1}{\varepsilon_{eq}} \int_0^{\varepsilon_{eq}} \left(\frac{\sigma_m}{\sigma_{eq}}\right) d\varepsilon_{eq} \quad (2)$$

In this technological and scientific context, this study may be considered as a primary attempt towards assessing the global formability of sheet metal flanging using SPIF within a wide range of parameters including flange widths and lengths, forming tool radii and step downs, among others. The selected material is AA2024-T3, a sheet aluminium alloy with low formability that is intensively utilized in the aeronautical industry. An intensive experimental campaign was carried out for evaluating the principal strain states on the final flanges using CGA. In addition, the finite element (FE) numerical modelling of the process was performed with the aim of providing a better understanding of the conditions that either permit the manufacturing of the flanged part or lead to failure in flanging by SPIF using concave dies. Furthermore, an analytical framework is provided for allowing the transformation of the material forming limits and the process loading paths from the principal strain space to the triaxiality space. From this overall perspective, formability and failure of stretch-flanging by SPIF is assessed and the capability of SPIF to enhance the inherently low formability of AA2024-T3 sheet is globally discussed.

2. Experimentation

This section contents the independent determination of the material forming limits by performing Nakazima tests, followed by the definition of an experimental plan within a wide range of parameters for the determination of formability and failure of stretch flanges deformed by SPIF. Every test presented in this section was carried out at least on 3 specimens for providing statistical meaning to the results obtained.

2.1. Mechanical characterization

The material considered in this study was AA2024-T3 aluminium alloy sheet of 1.2 mm thickness. This material presents a high strength but relatively low formability in cold

forming and it is extensively used in aeronautical applications such as the manufacturing of wing ribs, longerons, stringers, etc. Previous research of the authors on this material such as Vallellano et al (2008), as well as the recent investigation by López-Fernández et al. (2019) demonstrated its clear anisotropic behaviour, suggesting the characterisation of the new material batch by means of tensile tests along the rolling direction (RD - 0º), the transversal direction (90º) and the diagonal direction (45º). These tensile tests were carried out in accordance with the standards ASTM E8/E8M – 09 and ASTM E517 – 00, allowing to provide the tensile properties and anisotropy Lankford coefficients included in Table 1. The tensile stress-strain behaviour of the sheet material along the rolling direction follows the Eq. 3 where ε^p is the equivalent plastic strain. In addition, Figure 1 depicts the stress-strain curve for the three tested directions.

$$\bar{\sigma}(MPa) = 742.36(0.025 + \varepsilon^p)^{0.235} \tag{3}$$

Table 1. Mechanical properties including anisotropy coefficients along 0º (RD), 45º and 90º

Direction	σ_Y (MPa)	σ_{UTS} (MPa)	*E* (GPa)	*v*	$r_{0º\text{-}45º\text{-}90º}$
0º	336	526	69.4	0.33	0.76
45º	306		67.1		0.95
90º	319		68.2		0.54

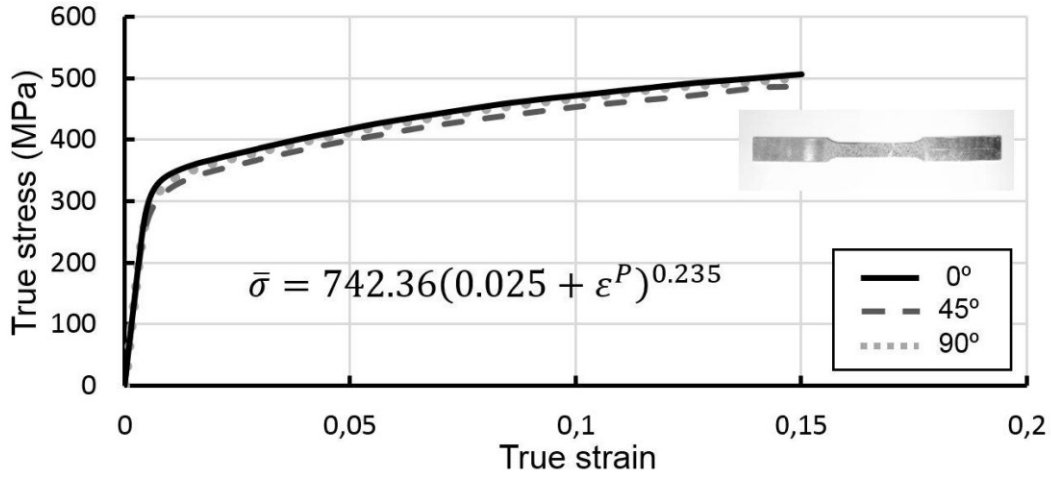

Figure 1. Stress-strain curve for different angles respect to the rolling direction

2.2. Forming limit diagram

With the aim of obtaining the material FLD, a series of Nakazima tests were carried out under the standard ISO 12004-2:2008. The experiments were conducted in a universal testing machine Erichsen® model 142-20 by using a hemispherical steel punch of 100 mm diameter, as is depicted in Figure 2. In order to assure minimum friction conditions, a set of Vaseline – PTFE – Vaseline was used in the interface between the punch and the specimen. As recommended in the standard, the punch velocity was set to 1 mm/s and the RD was oriented accordingly. The evolutions of principal strain distributions along the tests were captured using the Digital Image Correlation (DIC) system Aramis® version 6.3 with recording cameras of 1.3 Megapixels. The frame rate was set to 12 images per second and facet sizes of 13 x 11 pixels and overlapping were used (see Figure 2).

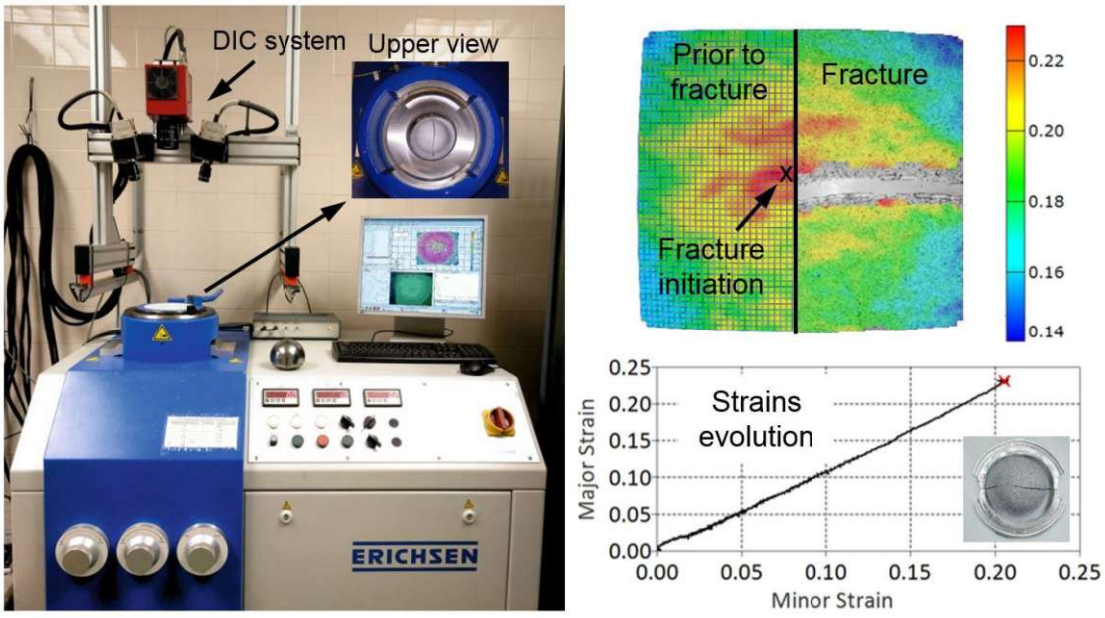

Figure 2. Erichsen® universal testing machine, evaluation of fracture strains using the system ARAMIS® and principal strains evolution of a Nakazima test close to equi-biaxial conditions

In order to obtain the material FLD depicted in Figure 3, a variety of strain paths from uniaxial straining towards biaxial conditions was considered by means of the five

testing specimen geometries, also shown in Figure 3. As it was expressed above, every test was reproduced at least 3 times with the aim of providing statistical meaning to the results presented. The methodology used for the evaluation of necking followed both (i) the ISO standard as well as (ii) the time-dependent methodology developed by the authors in Martínez-Donaire et al. (2014). Nevertheless, none of these methodologies revealed the appearance of any necking prior to fracture, as had been already observed by the authors in other batches of this low ductility material (López-Fernández et al. 2019). In addition, the observation of the thickness evolution close to the cracking line performed using optical microscopy agrees with the suggested mode of failure, which consists in ductile fracture attained directly in the absence of any necking (see the typical fracture morphology observed after cracking shown in Fig. 3).

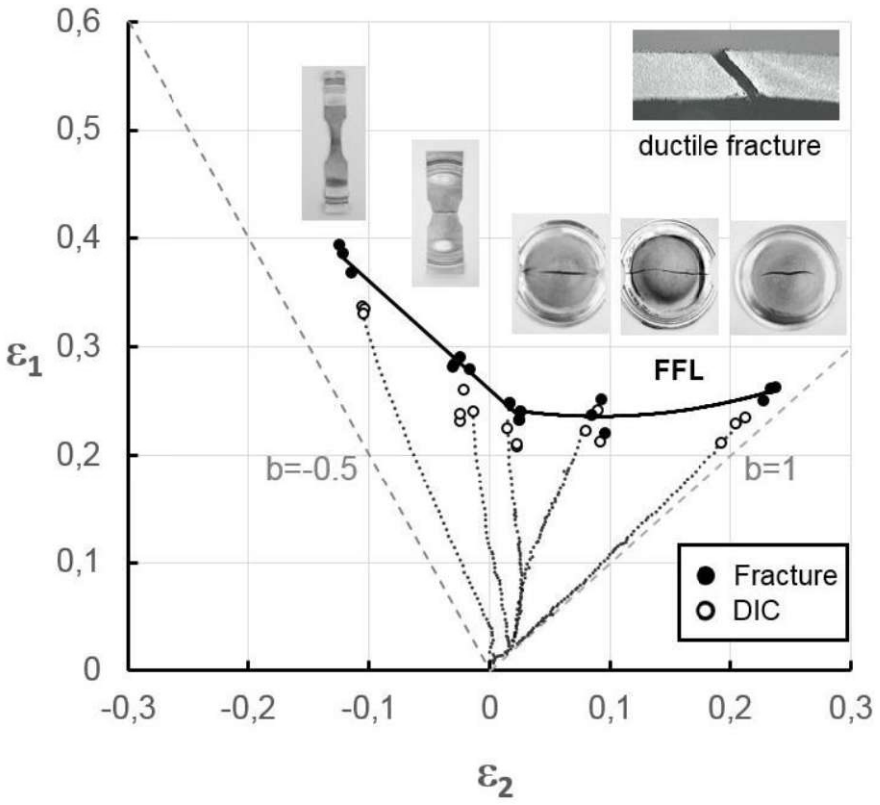

Figure 3. Forming limit diagram of the material represented uniquely by the FFL as a consequence of the type of failure consisting in direct ductile fracture in the absence of necking

Regarding the evaluation of the principal strains at fracture, and due to the difference in time between the last image recorded by Aramis® and the actual onset of fracture,

thickness was measured in the vicinity of the crack using a NICON® SMZ800 microscope analysed using KAPPA® Image Base Metreo version 2.7.2. Subsequently, the through thickness strain ε_3 was calculated assuming that the local strain path defined by the in-plane principal strains ratio β does not change significantly as fracture occurs, and thus can be assumed as constant (Eq. 4) and also applying volume constancy (Eq. 5).

$$\beta = \frac{\varepsilon_2}{\varepsilon_1} = \text{cte} \tag{4}$$

$$\varepsilon_{1,f} + \varepsilon_{2,f} + \varepsilon_{3,f} = 0 \tag{5}$$

where $\varepsilon_{3,f}$ is the average thickness strain evaluated in a series of points in the vicinity of the crack. Regarding to these results, fracture strains represented within the material FLD in Figure 3 correspond to the mode I of fracture mechanics (in-plane tension).

2.3. Stretch-flanging by SPIF

The experimental campaign in SPIF corresponds to the testing of stretch-flanges using a flexible setup with different concave radii (R_{die}) manufactured within a conventional CNC milling machine Emco® VMC 100 with the Emcotronic TM02 controller. Figure 4a represents a schematic representation of the flanging process whereas Figures 4b, 4c and 4d depict the experimental setup with an undeformed specimen, an actually manufactured stretch flange versus the initial specimen and the experimental setup showing a deformed stretch flange, respectively. Finally, Figure 4e shows the actual experimental set-up within the CNC machine after the manufacturing of a successful flange, describing the experimental devices and tool used for the tests. The metal sheet specimens were deformed by using a hemispherical spinning tool with a diameter Φ_{tool} describing circular arcs of Δz step down per pass, being the spindle speed S set to a constant value during the whole test. The feed rate was set to 1000 mm/min and the

lubrication was assured by applying neat forming oil Castrol Iloform TDN 81 as well as an air based cooling system that controls both the tool and the specimen temperature. In order to avoid premature failure, all specimens were polished at the edges prior to the test and a sheet of polytetrafluoroethylene (PTFE) was used in the interfaces between the dies and the sheet. Based on the industrial practice, it can be affirmed that small and medium radii flanges are more likely to fail than large radii. In this sense, flange radii of 20 mm and 45 mm were selected for defining the actual experimental campaign. In this regard, Table 2 shows the different values of the process parameters selected to perform the experiments. The principal strains were analysed off-line using the CGA system Argus®. This CGA measurement system is based on edging a pattern of circles on the undeformed specimen surface and measuring automatically the resulting ellipses once the sheet forming process is carried out. The system is able to evaluate the relative 3-D coordinates of the ellipses centres from a collection of photographs taken from different positions and angles, allowing to obtain the principal in-plane strains on the surface of the final specimen.

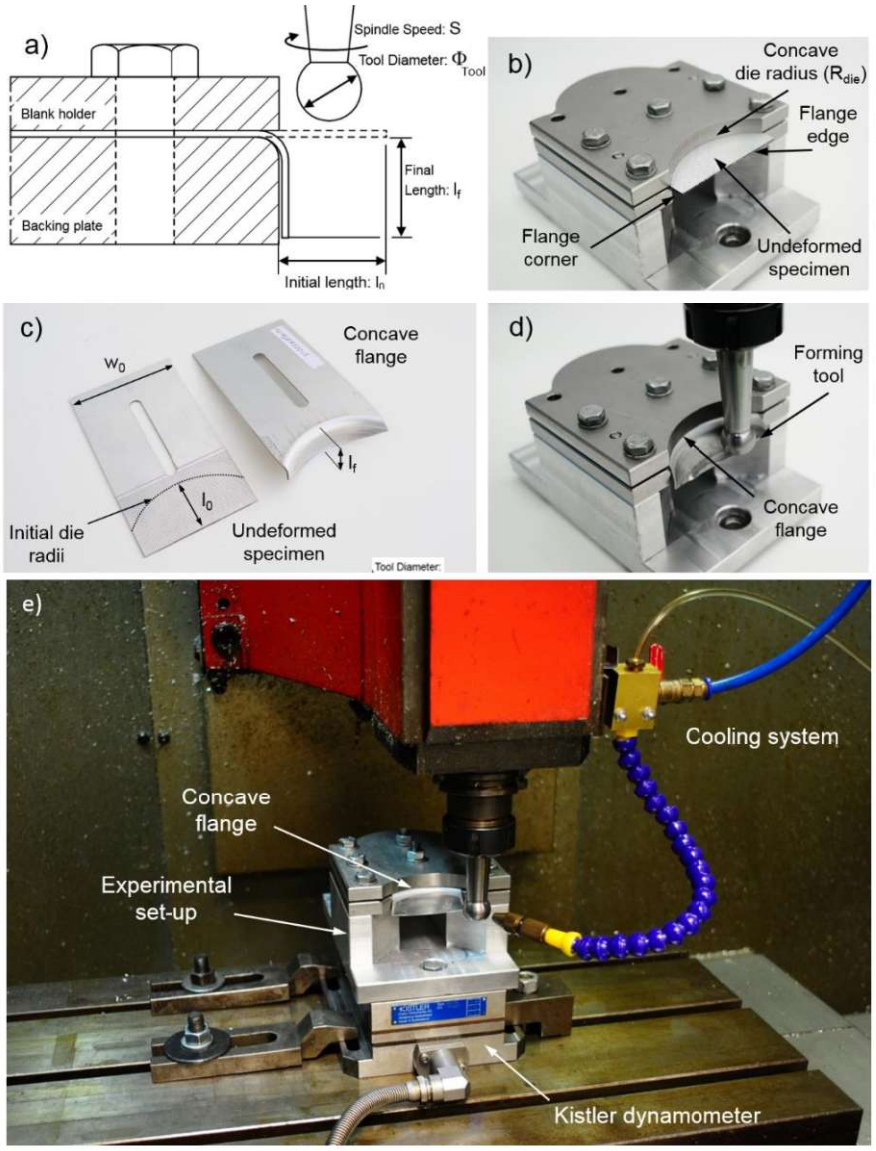

Figure 4. Stretch-flanging by SPIF: (a) Schematic representation of the process.
(b) Experimental setup with undeformed specimen,
(c) Undeformed specimen and stretch flange manufactured by SPIF,
(d) Experimental set up with forming tool and final flange,
(e) Actual experimental set-up within CNC machine

Table 2. Process parameter considered in the stretch-flanging experimental campaign

R_{die} (mm)	w_0 (mm)	l_o (mm)	S (rpm)	Φ_{tool} (mm)	Δz (mm)
45	36/ 45 / 54 / 63 / 72	15 / 20 / 25 / 30	20 / 1000	12 / 20	0.2 / 0.4
20	20 / 24 / 28 / 32 / 36				

Based on the different values of the process parameters provided in Table 2, Table 3 and Table 4 present the 87 different sets of parameters for a die radius R_{die} (see Figure 4b) of 45 mm and 20 mm respectively, defining the conditions of the same number of tests.

Notice that every experiment was performed a minimum of 3 times in order to provide statistical meaning, resulting in more than 200 stretch-flanging tests. The experiments carried out were based on the process parameters exposed above using initially a step down of 0.4 mm per pass, being the relevance of using Δz=0.2 mm discussed below.

The experiments are labelled using the following nomenclature: S (safe) for the cases of successfully manufactured flanges, and either F(E) (fracture at edge) or F(C) (fracture at corner) depending on the position were crack was observed. This nomenclature corresponds with the code of colours utilized in Table 3 and Table 4, representing in green the safe manufacturing zone, whereas yellow and red correspond to the failure zone by means of cracking either at the edge or at the corner (see Figure 4b), respectively. As exposed above, the consistency in terms of results was assured with at least 3 tests for each of the sets of process parameters considered.

In general terms, tests corresponding to short and narrow flanges (low values of w_0 and l_0) are within the safe zone, whereas higher values of w_0 and l_0 may lead to the fracture of the flanged sheet. Attending to the higher tool diameter Φ_{tool}, *i.e.* 20 mm, it increases the safe zone for $R_{die} = 45$ mm but it has the opposite effect for $R_{die} = 20$ mm, not providing a clear effect. In addition, a higher spindle speed $\boldsymbol{S}$ increases the success zone for both die radius, according with a similar trend previously obtained by the authors for hole-flanging of AA7075-O sheets in Borrego et al. (2016). In addition, it must be pointed out that, following the same good experimental practices used in Borrego et al. (2016), the cases of transition from no failure towards failure highlighted in Table 3 and Table 4 were repeated (at least 3 replicates) and analysed with special sensitivity with the aim of assuring the repetitively and statistical meaning of these

results, allowing establishing accurately the process windows for the stretch flanging process by SPIF.

For a better understanding of these results, a deeper analysis decreasing the forming tool to $\Phi_{tool} = 12$ mm on Table 3c will be carry out. In this table, for flanges with a width w_0 lower that 54 mm ($w_0 = 36$ and $w_0 = 45$) fracture does never occur as far as for narrow flanges the process is similar to a simple press-working sheet bending process performed by using a punch moving downwards. Additionally, the zone with a length l_0 lower that 25 mm ($l_0 = 15$ and $l_0 = 20$) is always within the safe zone as far as the flange length is too small to be stretched. Nevertheless, it have to be remarked that even though in the cases with low w_0 and high l_0 no cracks appeared, the resulting flange did not have the desired geometry due to springback effect. Moreover, it is also important to mention that for high w_0 and low l_0 the resulting flanges have a so small flange height that hardly has to adapt to the geometry of the die bending radius. On the other hand, within the unsafe zone corresponding to lower w_0 the predominant failure is fracture at corner or "F(C)". For this geometry, the flange is narrow enough to twist alternatively due to the tool-sheet friction actually producing cracking at the sheet corner due to the severe cyclic loading and the corresponding notable local plastic straining. This failure mechanism is directly related to the step down of the process because lower step downs means more alternative deformations for the same flange height. In this regard, many tests with $\Delta z = 0.2$ mm were performed to conclude that the safe zone increased for $\Delta z = 0.4$ mm because in some of these cases cracking at the corner can be avoid. This is by the way one of the main reasons of performing the final experimental plan focusing on a value of $\Delta z = 0.4$ mm. However, this cyclic straining is not equally severe for wider flanges as far as a high w_0 is related to stiffer flanges that are able to

avoid this alternative sheet twisting effect. Nevertheless, these flanges actually fail due to cracks produced by stretching in the middle zone of the flange edge, *i.e.* by "F(E)".

Table 3. Experiments corresponding to R_{die} = 45 mm

(a)	l_o (mm)	w_0 (mm)				
		36	**45**	**54**	**63**	**72**
Φ_{tool} = 20 (mm) S = 20 (rpm)	15				S	
	20			S	F(E)	S
	25	S	S	F(C)		F(E)
	30	S	S			

(b)	l_o (mm)	w_0 (mm)				
		36	**45**	**54**	**63**	**72**
Φ_{tool} = 20 (mm) S = 1000 (rpm)	15				S	
	20			S	F(E)	S
	25	S	S	F(C)		F(C)
	30	S	S			

(c)	l_o (mm)	w_0 (mm)				
		36	**45**	**54**	**63**	**72**
Φ_{tool} = 12 (mm) S = 20 (rpm)	15					
	20	S		S	S	**S**
	25	S	S	F(C)	F(C)	**F(E)**
	30	S	S			

(d)	l_o (mm)	w_0 (mm)				
		36	**45**	**54**	**63**	**72**
Φ_{tool} = 12 (mm) S = 1000 (rpm)	15					
	20	S	S	S	S	S
	25	S	S	F(C)	F(C)	S
	30	S	S			F(C)

S (Safe), F (failure) either at (C) corner or at the (E) edge.

Table 4. Experiments corresponding to R_{die} = 20 mm

(a)	l_o (mm)	w_0 (mm)				
		20	**24**	**28**	**32**	**36**
Φ_{tool} = 20 (mm) S = 20 (rpm)	15				S	S
	20	S	S	S	F(C)	F(C)
	25	S	S	S		

(b)	l_o (mm)	w_0 (mm)

		20	24	28	32	36
Φ_{tool} = 20 (mm)	15				S	S
S = 1000 (rpm)	20	S	S	S	F(C)	F(C)
	25	S	S	S		

(c)

l_o (mm)	w_0 (mm)				
	20	24	28	32	36
15		S	S	**S**	**F(E)**
20	S	S	S	S	F(C)
25	S	S	S	F(C)	

Φ_{tool} = 12 (mm), S = 20 (rpm)

(d)

l_o (mm)	w_0 (mm)				
	20	24	28	32	36
15					S
20	S	S	S	**S**	F(E)
25	S	S	S	**F(C)**	

Φ_{tool} = 12 (mm), S = 1000 (rpm)

S (Safe), F (failure) either at (C) corner or at the (E) edge.

In the following sections, a more detailed discussion on the formability and failure of the stretch flanges deformed by SPIF exposed in Table 3 and Table 4 will be carried out in terms of the principal strains provided by the CGA system Argus®. In this sense, Figure 5 depicts an example of the Argus® analysis performed on a formed stretch flange (Figure 5a) providing the principal strains on the outer face of the flange (opposite face to the one touched by the tool) in the principal strain diagram (Figure 5b). The contours of major and minor in-plane principal strains are depicted in Figure 5c and 5d.

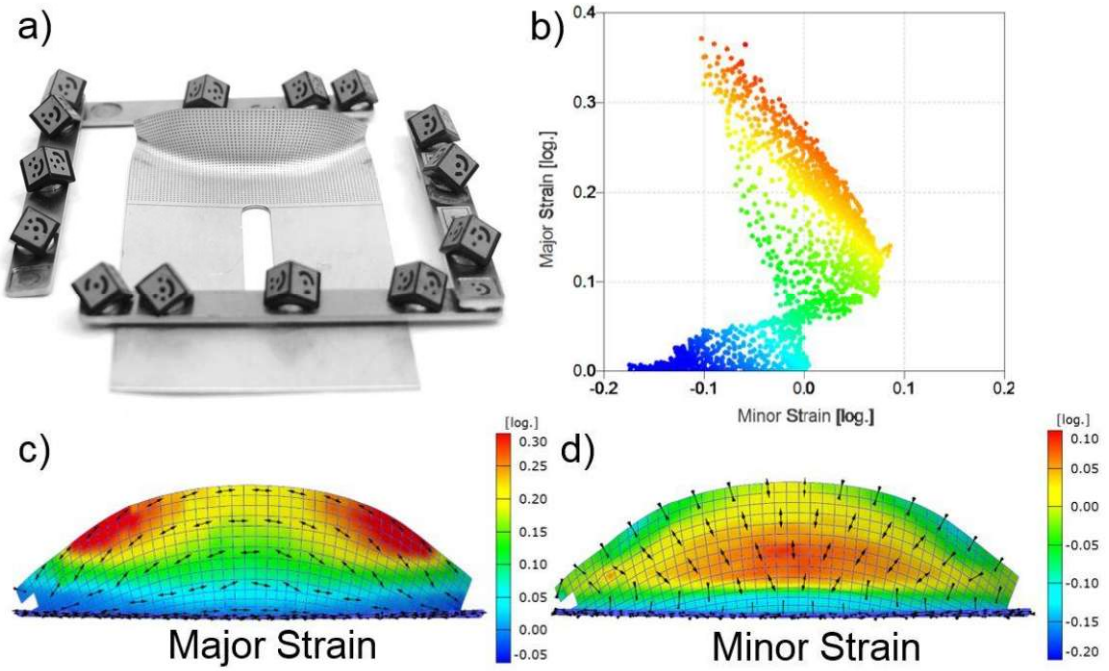

Figure 5. Strain measurement using CGA Argus® (a) Example of a flange measurement, (b) major strain versus minor strain depicting selected sections, (c) Contour of major and (d) minor strain depicting a central (black) and a lateral (blue) selected sections

Finally, it must be pointed out that the actual geometry of the flange edge is not straight (see Figure 5a), as could be expected for most industrial applications. This is an obvious consequence of considering for simplicity reasons a circular pre-cut of the sheet blank testing geometry. Indeed, the main objective of this preliminary research work is the assessment of formability and failure and thus, this issue is not crucial in this case. Nevertheless, the authors are working in the development of optimized blank geometries for obtaining final flanges with straight edges without needing any further finishing operation such as machining. These results will be exposed in future research work.

3. Numerical modelling

With the aim of providing a better understanding of the stress/strain states controlling formability and failure in stretch flanging by single point incremental forming, an

explicit Finite Element (FE) model was developed by using the explicit time integration software Ansys LS-DYNA® V19.1. The numerical model is necessary for performing the analysis of the results in terms of stress triaxiality carried out in section 5 as well as for optimizing the initial geometry that had to be machined to the undeformed metal sheet specimens.

The FE model was developed by using the solid-shell element type Solid SHELL163 selected from the LS-DYNA elements library. These 4-node elements were used in combination with the Belytschko-Tsay formulation and Reissner-Mindlind kinematic assumption with five integration points through the sheet thickness and hourglass control, as exposed in the ANSYS/LS-DYNA V19.1 User's Guide. The material behaviour was defined based on the Barlat-89 (Barlat and Lian, 1989) elastic-plastic rate independent plasticity model with isotropic hardening and following a Swift power law. The punch and the dies were modelled as rigid bodies and surface-to-surface contact with Coulomb friction (μ=0.01) was set in the contact region between the tool and the sheet. This value was tuned by comparing numerical results with experimental results in terms of the contour of principal strains and the forming force evolutions. Sheet, punch and dies were meshed using a regular mesh with characteristic length ranging between 0.5 and 1.5 mm. The total number of elements depends on the geometrical dimensions of each case, being around 1000 elements for the smallest and 4000 for the largest model. The values of the parameters used for defining the FE modelling are provided in Table 5.

Table 5. Parameters defining the numerical model.

Formulation	Belytschko-Tsay	**Element size (mm)**	0.5 – 1.5
Material model	Barlat-89	**Hourglass control**	Stiffness method
LS Dyna element	SHELL163	**Hourglass coeff.**	0.01

type			
Barlat Exponent	8	**Friction coeff.**	0.01
Mass Scaling	5	**Time scaling**	500

Figure 6a depicts the initial Finite Element modelling showing the regular initial meshing of the sheet whereas Figure 6b depicts the contour of the major strain on the outer surface of the deformed specimen corresponding to a characteristic case of the stretch flanging process simulated using Ansys.

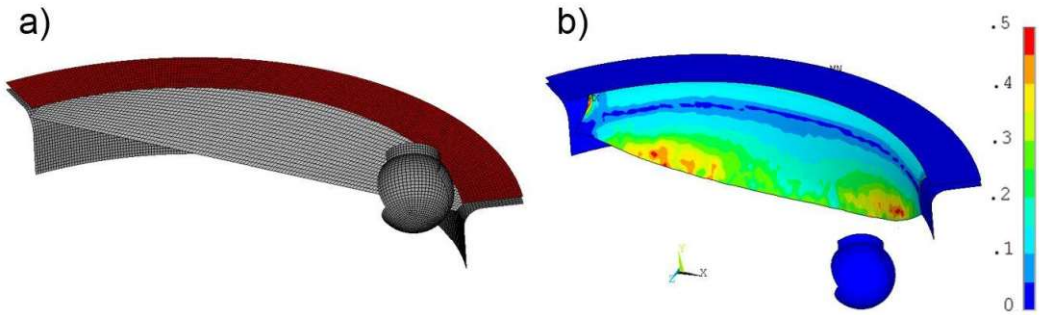

Figure 6. (a) FE modeling and (b) numerical contour of major strain on the final flange

In order to reduce the computational cost, mass and time scaling were used after verifying that the results were similar to those obtained in the non-scaled model. This assumption allowed to obtain a solution for the largest model in about 8 hours of CPU time instead of the 5 days needed in the case of the non-scaled model. The computer used was equipped with 8 CPUs Intel® Xeon E3 v6 (3GHz) processors and 32 Gb of RAM memory.

4. Analytical framework

The transformation of the experimental loading paths and the corresponding forming limits from the space of principal strains towards the space of triaxiality, representing effective strain versus stress-triaxiality, requires evaluating the effective stress $\bar{\sigma}$, the average stress σ_m and the effective strain $\bar{\varepsilon}$ at the locations in which experimental strain loading paths were determined. This space transformation is built upon the non-

quadratic Barlat-89 (Barlat and Lian, 1989) plasticity criterion, assuming proportional loading and plane stress deformation ($\sigma_t = \sigma_3 = 0$) along the thickness direction.

The above mentioned non-quadratic Barlat-89 plasticity criterion was originally derived for anisotropic metal sheet and assumes planar anisotropy and the principal axes of the stress and strain tensors to coincide at each point, as exposed in Eq. 6.

$$2\sigma_Y^m = a|K_1 + K_2|^m + a|K_1 - K_2|^m + c|2K_2|^m \tag{6}$$

where, K_1 and K_2 (Eq. 7 and Eq. 8) are function of the principal stresses σ_1 and σ_2, which are related by the definition of alpha provided in Eq. 9.

$$K_1 = \frac{\sigma_1 + h\sigma_2}{2} = \frac{(1 + h\alpha)\sigma_1}{2} \tag{7}$$

$$K_2 = \sqrt{\left(\frac{\sigma_1 - h\sigma_2}{2}\right)^2} = \sqrt{\left(\frac{(1 - h\alpha)\sigma_1}{2}\right)^2} \tag{8}$$

$$\alpha = \frac{\sigma_2}{\sigma_1} \tag{9}$$

being the parameters a, c, and h given by Eq. 10, Eq. 11 and Eq. 12 respectively, which have been determined using the coefficients of anisotropy r_0 at 0° (longitudinal) and r_{90} at 90° (transversal) with respect to the rolling direction. Additionally, the exponent m depends on the crystalline structure of the material and is usually set to 8 in face centred cubic (FCC) and 6 in body centred cubic (BCC) structures.

$$a = 2 - 2\sqrt{\frac{r_0}{1 + r_0} \cdot \frac{r_{90}}{1 + r_{90}}} \tag{10}$$

$$c = 2 - a \tag{11}$$

$$h = \sqrt{\frac{r_0}{1 + r_0} \cdot \frac{1 + r_{90}}{r_{90}}} \tag{12}$$

Considering the general flow rule expressed in Eq. 13,

$$d\bar{\varepsilon}_{ij} = d\lambda \frac{\partial f(\sigma_{ij})}{\partial \sigma_{ij}} \tag{13}$$

where $d\lambda > 0$ is an instantaneous hardening parameter related to the material strain - stress curve and $f(\sigma_{ij})$ is taken as the Barlat-89 plasticity criterion, the expressions in Eq. 14 and Eq. 15 are obtained for $d\varepsilon_1$ and $d\varepsilon_2$,

$$d\varepsilon_1 = am|K_1 + K_2|^{m-2}(K_1 + K_2) + cm|2K_2|^{m-2}(2K_2) \tag{14}$$

$$d\varepsilon_2 = amh|K_1 - K_2|^{m-2}(K_1 - K_2) - cmh|2K_2|^{m-2}(2K_2) \tag{15}$$

and consequently the stress ratio $\beta = \frac{d\varepsilon_2}{d\varepsilon_1}$ can be expressed as follows,

$$\beta = \frac{am|K_1 + K_2|^{m-2}(K_1 + K_2) + cm|2K_2|^{m-2}(2K_2)}{amh|K_1 - K_2|^{m-2}(K_1 - K_2) - cmh|2K_2|^{m-2}(2K_2)} \tag{16}$$

Using the values of K_1 and K_2 expressed in Eq. 7 and Eq. 8, Eq. 16 results as follows:

$$\beta = \frac{ah\left|\frac{(1+h\alpha)}{2} - \sqrt{\left(\frac{(1-h\alpha)}{2}\right)^2}\right|^{m-2}\left(\frac{(1+h\alpha)}{2} - \sqrt{\left(\frac{(1-h\alpha)}{2}\right)^2}\right) - ch\left|2\sqrt{\left(\frac{(1-h\alpha)}{2}\right)^2}\right|^{m-2}\left(2\sqrt{\left(\frac{(1-h\alpha)}{2}\right)^2}\right)}{a\left|\frac{(1+h\alpha)}{2} + \sqrt{\left(\frac{(1-h\alpha)}{2}\right)^2}\right|^{m-2}\left(\frac{(1+h\alpha)}{2} + \sqrt{\left(\frac{(1-h\alpha)}{2}\right)^2}\right) + c\left|2\sqrt{\left(\frac{(1-h\alpha)}{2}\right)^2}\right|^{m-2}\left(2\sqrt{\left(\frac{(1-h\alpha)}{2}\right)^2}\right)} \tag{17}$$

Then, considering the incremental plastic work per unit of volume expressed as in Eq. 18,

$$dw_p = \sigma_1 d\varepsilon_1 + \sigma_2 d\varepsilon_2 = \bar{\sigma} d\bar{\varepsilon} \tag{18}$$

substituting the strain differentials of Eq. 14 and Eq. 15 in Eq. 16, and assuming the equivalent stress obtained from Eq. 6, the effective strain increment $d\bar{\varepsilon}$ becomes,

$$d\bar{\varepsilon} = \frac{\sigma_1 d\varepsilon_1 + \sigma_2 d\varepsilon_2}{\bar{\sigma}} = \frac{(1 + \alpha\beta)\sigma_1 d\varepsilon_1}{\bar{\sigma}} =$$

$$= \frac{(1 + \alpha\beta)d\varepsilon_1}{\left(\frac{a}{2}\left|\frac{(1+h\alpha)}{2} + \sqrt{\left(\frac{(1-h\alpha)}{2}\right)^2}\right|^m + \frac{a}{2}\left|\frac{(1+h\alpha)}{2} - \sqrt{\left(\frac{(1-h\alpha)}{2}\right)^2}\right|^m + \frac{c}{2}\left|\sqrt{(1-h\alpha)^2}\right|^m\right)^{\frac{1}{m}}} \tag{19}$$

Which is also valid in terms of absolute variables $\bar{\varepsilon}_{eq} = f(\varepsilon_1)$ under the assumption of proportional loading.

Finally, expressing the mean stress σ_m in plane stress conditions ($\sigma_3 = 0$) as follows:

$$\sigma_m = \frac{\sigma_1 + \sigma_2 + \sigma_3}{3} = \frac{\sigma_1 + \sigma_2}{3} = \frac{1+\alpha}{3}\sigma_1 \tag{20}$$

it is possible to use the Eq. 6 and Eq. 20 to define the stress triaxiality ratio η as follows,

$$\eta = \frac{\sigma_m}{\bar{\sigma}} = \tag{21}$$

$$= \frac{\frac{(1+\alpha)}{3}}{\left(\frac{a}{2}\left|\frac{(1+h\alpha)}{2} + \sqrt{\left(\frac{(1-h\alpha)}{2}\right)^2}\right|^m + \frac{a}{2}\left|\frac{(1+h\alpha)}{2} - \sqrt{\left(\frac{(1-h\alpha)}{2}\right)^2}\right|^m + \frac{c}{2}\left|\sqrt{(1-h\alpha)^2}\right|^m\right)^{\frac{1}{m}}}$$

Eq. 19 and Eq. 21 will be used to transform the proportional strain loading paths and the forming limits from the space of principal strains to the space of triaxiality using, for the first time ever, the Barlat-89 plasticity criterion. Recently, related to previous work of the authors focused in the evaluation of formability and failure of thin-walled tubes (Magrinho et al, 2019a; Cristino et al., 2020), Magrinho et al (2019b) proposed the analytical transformation between both spaces using Hosford yield criterion for proportional loading, based on the previous work by Martinez Donaire et al. (2019), where the mapping equations for the Hill yield criterion including the kinked strain path experimentally observed in Nakazima tests was derived.

In addition to that, as it was exposed by Martins et al (2014), it is generally assumed that failure in SPIF is usually attained in mode I of fracture mechanics coinciding with

in-plane tension.In this regard, the damage function by Atkins (1996) derived from the void-growth-by-dilatation McClintock (1968) criterion provided by Eq. 1 can be expressed in terms of the average triaxiality ratio $\bar{\eta}$ (defined in Eq. 2), as exposed in Eq. 22:

$$D_{void} = \int_0^{\bar{\varepsilon}} \frac{\sigma_m}{\bar{\sigma}} d\bar{\varepsilon} = \bar{\eta}\bar{\varepsilon} \tag{22}$$

Indeed, as discussed in section 1 recent studies as Mirnia and Shamsari (2017) and Martinez Donaire et al. (2019) pointed out the importance of considering the average stress triaxiality for a precise evaluation of the sheet formability and failure in ISF processes. In this sense, the average stress triaxiality expressed in Eq. 2 should consider the calculated expressions of the mean and the equivalent plastic strains corresponding to the Barlat-89 criterion resulting in the triaxiality ratio Eq. 21, allowing to integrate it for finally obtaining the average triaxiality ratio as exposed in Eq. 23:

$$\bar{\eta} = \frac{1}{\bar{\varepsilon}_f} \int_0^{\bar{\varepsilon}_f} \frac{\sigma_m}{\bar{\sigma}} d\bar{\varepsilon} \tag{23}$$

Notice that in case of an ideal proportional forming process, the stress triaxiality and the average stress triaxiality do coincide.

5. Results and discussion

This section aims discussing the results obtained including (i) a first subsection analysing some selected cases of the stretch flanging process by SPIF in terms of principal strains, followed by (ii) a second subsection including the validation of the numerical modelling using experimental results in order to being finally able, in the third subsection, to (iii) evaluate the process formability and failure within the

equivalent plastic strain versus stress triaxiality space, by using the average stress triaxiality as was previously discussed.

5.1. Principal strain space analysis

The analysis within the principal strain space will focus on some selected cases in the transition from the successful manufacturing of a stretch-flanging by SPIF towards its failure by fracture (cases highlighted in bold in Table 3c and Table 4c). The overall aim of this study is to understand the conditions upon which failure is attained, and thus limiting the safe formability zone of the process related to the set of process parameters considered. Indeed, the four selected tests correspond to fixed values of 12 mm of tool diameter and 20 rpm of spindle speed, whereas the die radii are $R_{die} = 45$ mm and $R_{die} = 20$ mm, respectively. In the former case ($R_{die} = 45$ mm) the transition from a successful flange towards failure F(E) is attained and analysed vertically in Table 3, *i.e.* for a constant value of the flange width w_0, whereas in the latter case ($R_{die} = 20$ mm) this transition towards failure at edge F(E) is attained horizontally, i.e. for a constant value of flange length l_0. The analysis focused on these 4 tests as they are considered as the most representative cases to illustrate the influence of the principal strains on the formability in stretch flanging by SPIF compared to formability and the material fracture forming limit (FFL) accomplished in conventional Nakazima testing for the AA2024-T3 sheet.

First, focusing on $R_{die} = 45\ mm$, the selected cases are of 72 mm width ($w_0 = 72\ mm$) and initial lengths of 20 and 25 mm ($l_0 = 20$ and $l_0 = 25\ mm$), corresponding with a successful flange and a specimen attaining fracture, respectively.

In this regard, Figure 7a depicts for a flange of 20 mm length (successful flange) the contour of thickness reduction obtained using Argus®. Figure 7c presents the corresponding contour of major versus minor principal strains of the flange within the FLD along with the FFL of the material. The most representative section (where fracture usually occurs in not successful cases) has been presented in the thickness contour in blue colour (Figure 7a) and in the FLD with a white-circle dotted line (Figure 7c). The last point of this section correspond to the strain measurement at the edge of the flange obtained by measuring the thickness at the flange edge using optical microscopy assuming volume constancy and forcing this point to be in pure tension that is $\beta = -0.43$ according to Barlat-89 yield criterion.

Analogously, Figure 7b and Figure 7d represent for the case of 25 mm of initial flange length (corresponding to a failure-at-edge F(E) specimen) the contour of thickness reduction obtained using Argus® and the corresponding contour of major versus minor principal strains of the resulting fractured flange, respectively. In addition to the former case, Figure 7d shows a detail of the fractured edge obtained using optical microscopy and the corresponding principal strain state represented through a black diamond.

It is worth mentioning that the maximum thickness reduction levels are higher in the case of the fractured specimen (Figure 7b) than in the case of the successful flange (Figure 7a). In addition, the maximum levels of principal strains are slightly above the FFL in the case of the successful flange (as can be seen in Figure 7c), whereas in the case of fracture the maximum level of principal strains are significantly above the FFL, although in this latter case this could be achieved through unexpected deformation in the vicinity of the crack. Nevertheless, in the case of the successful flange ($l_0 = 20$) but also in the case of the fractured flange ($l_0 = 25\,mm$) well outside of the zone of

fracture, it is possible to see a substantial number of points where the principal strains attained are above the FFL, demonstrating the increase in formability of the flanging process by SPIF. Similar results including spifability within the material FLD above the conventional FFL obtained via Nakazima tests have been reported in previous research work by the authors and their collaborators for aluminium sheet (Martinez Donaire et al., 2019) but also for other materials such as stainless steel sheet of AISI 304-H111 (Centeno et al., 2014).

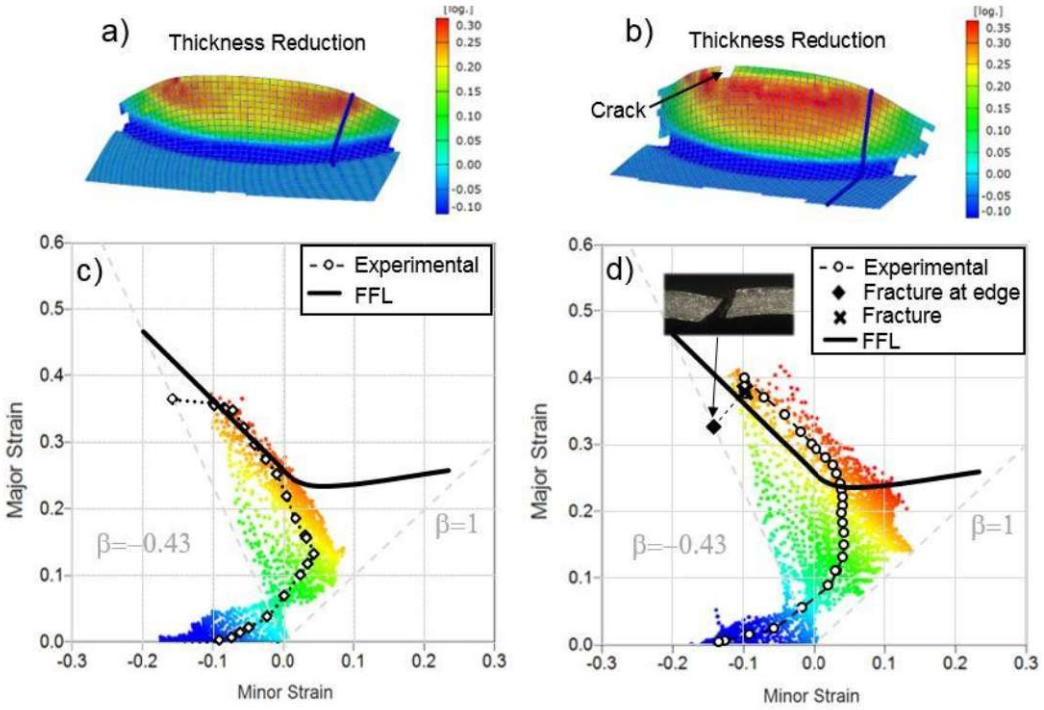

Figure 7. Analysis of formability and failure in stretch flanging performed with $\phi_{tool} = 12$ mm, $w_0 = 72$ mm and a forming die of $R_{die} = 45$ mm: (a) Contour of thickness reduction for an initial flange length of $l_0 = 20$ mm and (b) $l_0 = 25$ mm, respectively. (c) Global strain pattern (colored dots) and strain evolution along the central section (black circles) for a flange corresponding to an initial flange length of $l_0 = 20$ mm and (d) $l_0 = 25$ mm vs. the FFL, respectively.

Likewise, the previous analysis was also performed for the two specimens corresponding to a stretch-flanging die of $R_{die} = 20$ mm, related in this case to an initial flange length of $l_0 = 15$ mm and initial widths of the specimens of $w_0 = 32$ mm and $w_0 = 36$ mm, corresponding with a successful flange and a specimen attaining fracture at edge or F(E), respectively (as shown in Table 4c highlighted in bold). In this

sense, Figure 8 presents the combined analysis of formability and failure for these 2 selected cases.

Figure 8a depicts the contour of thickness reduction obtained using Argus® for the successful flange corresponding to an initial width of $w_0 = 32$ mm. In this case, the most representative section is located by the central zone of the flange, being this the location where fracture usually occurs. The most representative section represented in blue colour (Figure 8a) corresponds in the FLD with a white-circle dotted line (Figure 8c). It can be observed that the points with higher levels of strains are slightly below the FFL whereas the last point of the section, located at the edge of the flange, is in uniaxial tension. In the case of failure (Figure 8b), the fracture was located by the central section and in the very edge of the flange (point represented with 'x') coinciding with the zone of higher thickness reduction. Finally, Figure 8d represents the strain distribution of the failed specimen within the FLD. The fracture point represented with a black diamond was measured using the same criteria that in the failure case of $R_{die} = 45$ mm. Even when in this case of $R_{die} = 20$ mm there are not a number of points above the FFL, the levels of principal strains are higher than in the case of no failure, existing a certain number of points with levels of strains above the conventional limit.

To sum up, it must be noticed that comparing the four specimens corresponding to the 2 different die radii considered, it can be concluded that the smaller die radii favours close to plane strain states in the flanges whereas the specimens with higher die radii have a strain distribution that comprehends strain states close to plane strain but also other states corresponding to a wider range of beta values.

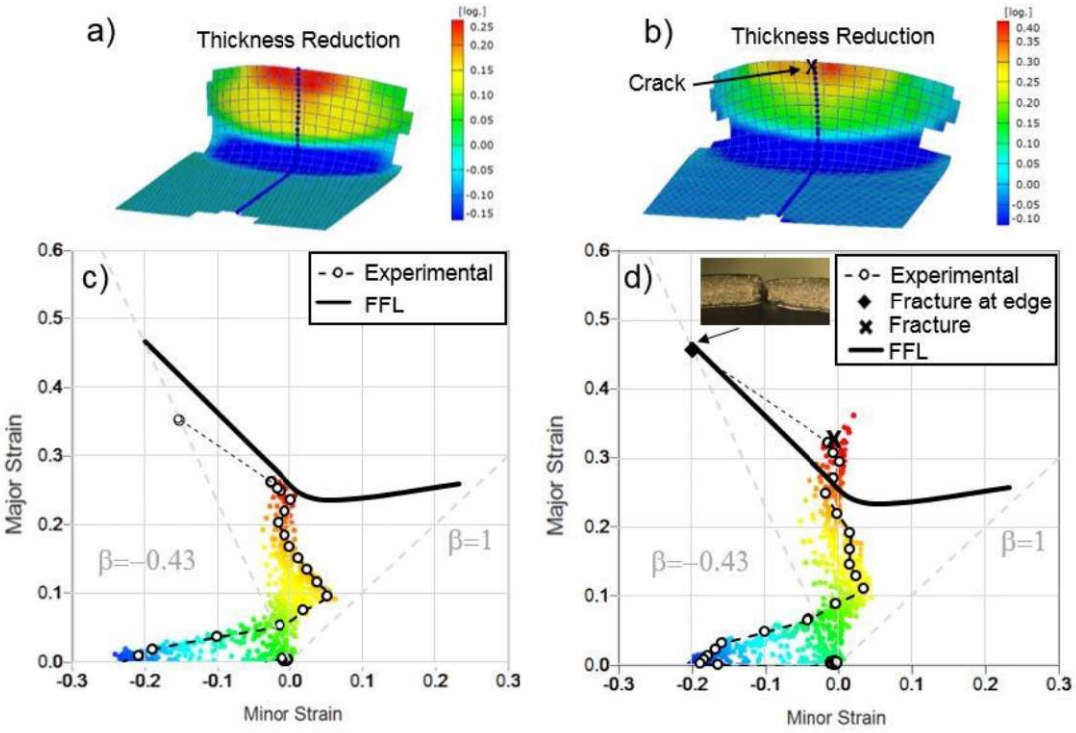

Figure 8. (a) Thickness reduction contour for $w_0 = 32$ mm. (b) Thickness reduction for $w_0 = 36$ mm. (c) Global strain pattern (colored dots) and strain evolution along the central section (black circles) for a flange with $w_0 = 32$ vs. the FFL. (d) *idem* for a fractured flange with $w_0 = 36$. (All the figures correspond to $\phi_{tool} = 12$ mm, $l_0 = 15$ mm and $R_{die} = 20$ mm).

5.2. Validation of the numerical model

In this section, the results provided by the finite element modelling are analysed and validated in terms of principal strains by comparing them with the previously exposed experimental results. With this aim, 4 numerical models are developed for reproducing the 4 experiments described in section 5.1 and the resulting numerical contours of principal strains are compared with the corresponding experimental data, focusing especially in the strain distributions along the most representative sections presented. This validation in terms of strains has been successfully used in previous studies such as Centeno et al. (2017).

In this regard, Figure 9a and 10a represent the comparison of the principal strains corresponding to the non-failure and failure cases selected for $R_{die} = 45$ mm together

with the material FFL. As can be seen, for both cases there exist a good agreement of the numerical with the experimental results, thus allowing to use the numerical model to provide accurate strain values as well as to predict the onset of fracture. Furthermore, in order to visualize the previous validation, the corresponding experimental and numerical contours of major strain are depicted in Figure 9b.1 and Figure 9b.2 for the non-failure case as well as in Figure 10b.1 and Figure 10b.2 for the case of the fractured flange. In both cases, the distribution of strains is very similar, showing again a good agreement of the numerical model with the experimentation.

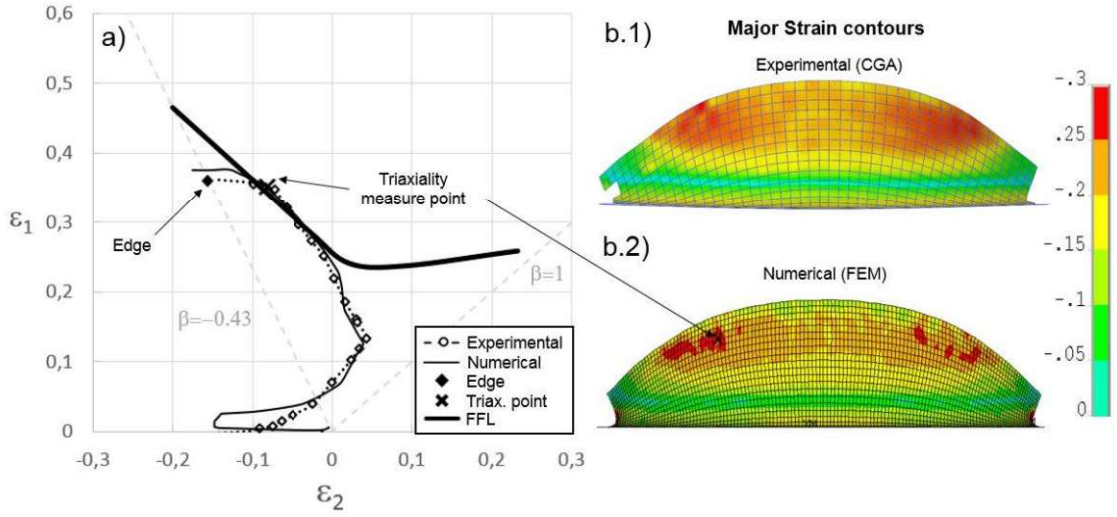

Figure 9. Validation of numerical modelling: (a) Comparison of numerical vs. experimental principal strains. Contour of major strain (b.1) Experimental and (b.2) Numerical (The figures correspond to non-failure case $\phi_{tool} = 12$ mm, $l_0 = 20$ mm and $R_{die} = 45$ mm and $w_0 = 72$).

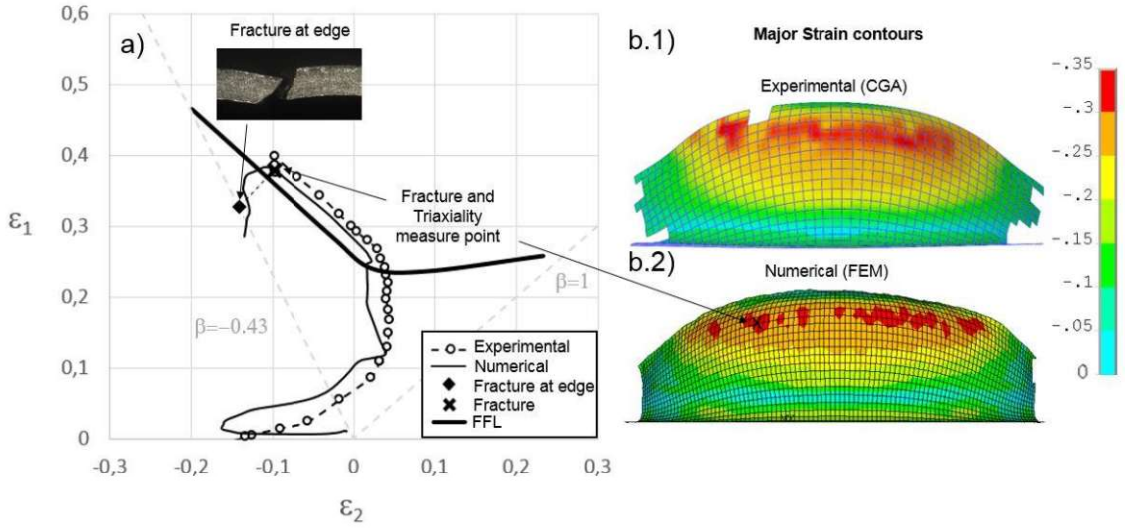

Figure 10. Validation of numerical modelling: (a) Comparison of numerical vs. experimental principal strains. Contour of major strain (b.1) Experimental and (b.2) Numerical (The figures correspond to the failure case $\phi_{tool} = 12$ mm, $l_0 = 25$ mm and $R_{die} = 45$ mm and $w_0 = 72$).

Analogously, a similar validation of the numerical modelling was performed for the case of $R_{die} = 20$ mm providing the results shown in Figure 11 and Figure 12. In this case, the numerical results in terms of principal strains where evaluated at the corresponding sections by the central zoned of the flange. As can be concluded, the results provided by the numerical modelling are again consistent, demonstrating that the numerical models developed are able to accurately reproduce the stretch flanging process. In this regard, it can be seen that the numerical strains evaluated at the corresponding sections are below the FFL curve in the case of the non-failure specimen whereas they are slightly above this forming limit in the case of the specimen attaining fracture, reproducing the experimental observations. Once again, the experimental and numerical contours of major strain are provided in Figure 11b.1, Figure 11b.2, Figure 12b.1 and Figure 12b.2 for the cases of no failure and fracture respectively. As can be observed, these results in terms of major strain distribution justify once again the consistency of the numerical model developed.

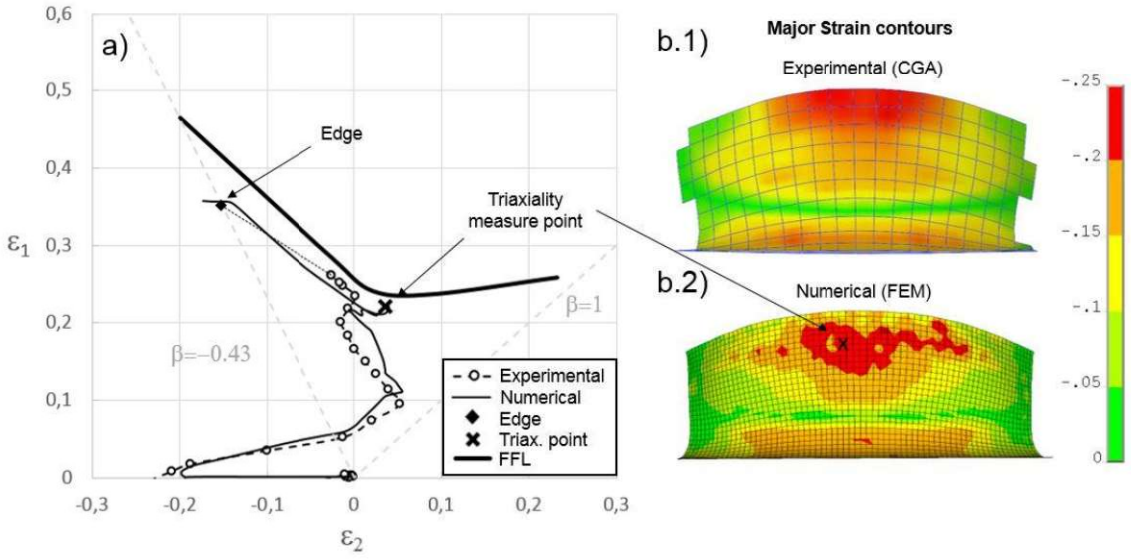

Figure 11. Validation of numerical modelling: (a) Comparison of numerical vs. experimental principal strains. Contour of major strain (b.1) Experimental and (b.2) Numerical (The figures correspond to non-failure case $\phi_{tool} = 12$ mm, $l_0 = 15$ mm and $R_{die} = 20$ mm and $w_0 = 32$).

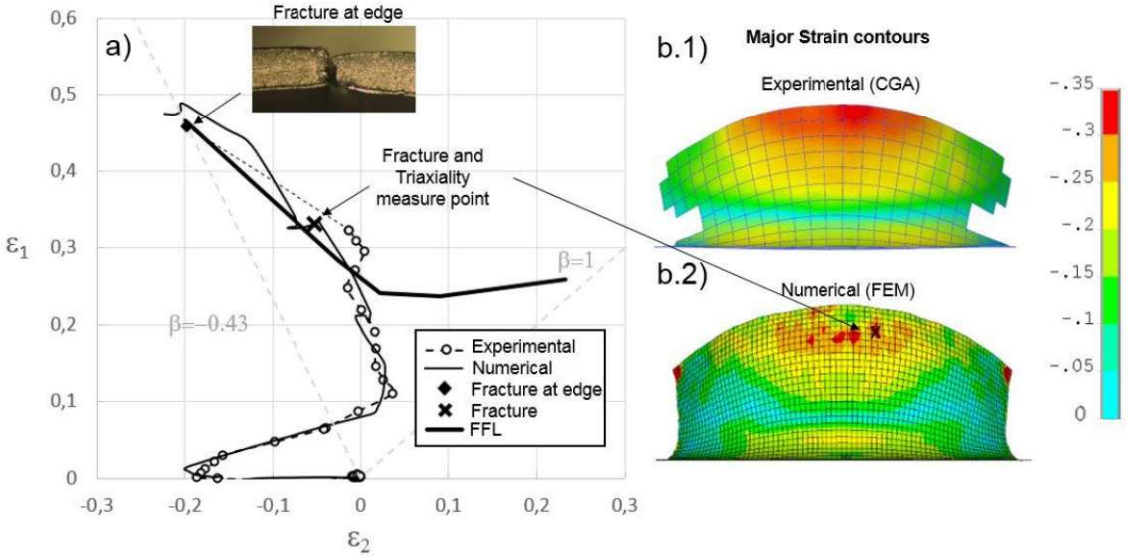

Figure 12. Validation of numerical modelling: (a) Comparison of numerical vs. experimental principal strains. Contour of major strain (b.1) Experimental and (b.2) Numerical (The figures correspond to the failure case $\phi_{tool} = 12$ mm, $l_0 = 15$ mm and $R_{die} = 20$ mm and $w_0 = 36$).

5.3. Analysis within the equivalent strain versus stress triaxiality space

As a consequence of the results exposed in sections 5.1 and 5.2, it must be clear that the increase of formability attained in stretch flanging by SPIF cannot be uniquely explained by the conventional forming approach based on the use of the FLD, as far as based on this approach the FFL would be the limit beyond which higher levels of principal strains should not be reached. With the objective of providing a more suitable explanation, the methodology exposed by the authors in Martinez Donaire et al. (2019), here particularised by using the Barlat-89 anisotropy criterion, is used to carry out an analysis within the space of equivalent strain versus stress triaxiality both for proportional and non-proportional loading in order to evaluate the effect of the stress triaxiality on the enhancement of formability observed.

First, the experimental results of Nakazima tests providing the FFL within the principal strain space were transformed under the assumptions of the analytical framework described above (section 4) in order to obtain the FFL within the stress triaxiality space. The equivalent strains (ε_{eq}) at fracture were obtained from the corresponding experimental values of the principal strains at fracture, whereas the values of average stress triaxiality for these experiments were obtained from the corresponding numerical models reproducing the above mentioned Nakazima tests and assuming that the end of each numerical simulation coincides with the instant in which the experimental strains at fracture are attained. Under these circumstances, depending of the selected plasticity criterion, a different FFL curve within the triaxiality space is obtained in Figure 13. The black curve corresponds to the Barlat-89 anisotropic plasticity criteria (see section 4 for further details). Additionally, the grey curve represents the FFL curve by assuming the Von Mises isotropic plasticity criterion as a reference. It is worth mentioning that in Nakazima tests the local stress triaxiality η is almost identical to the averaged stress triaxiality $\bar{\eta}$ since the strain paths correspond to almost proportional loading. Besides, in the case of assuming isotropic plasticity, the uniaxial tension test corresponds to $\bar{\eta} = 0.33$, and the plane strain and equi-biaxial strain points correspond to $\bar{\eta} = 0.58$ and $\bar{\eta} = 0.67$ respectively. In the case of taking anisotropy into account by using the Barlat-89 yield criteria, these values expressed in the same order as for isotropic materials correspond to $\bar{\eta} = 0.33$, $\bar{\eta} = 0.53$ and $\bar{\eta} = 0.65$, respectively.

Figure 13 provides the analysis of the flanging process within the triaxiality space showing the evolution along the flanging process of equivalent strain versus average stress triaxiality for the cases of a successful flange (blue curve) versus a failed flange (red curve) corresponding to $R_{die} = 20$ mm (Figure 13a) and $R_{die} = 45$ mm die radius

(Figure 13b), respectively. The location where the numerical variables (i.e. equivalent strain and stress triaxiality) has been evaluated in each case coincide with the previously selected and depicted in Figure 9 to Figure 12 labelled with an 'x'. These locations have been chosen coinciding with the fracture zones in the case of a failure and do correspond with the point reaching the highest value of equivalent strain in the case of no failure.

As can be seen, for both die radii analysed, no mattering whether the test corresponds to a failure specimen or not, the values of equivalent strain ε_{eq} are sensibly higher than the FFL curve obtained using the Barlat-89 criteria. At the same time, the values of average stress triaxiality $\bar{\eta}$ are always sensibly lower that the values obtained in the case of Nakazima tests. It can be clearly inferred that the flanging process via single point incremental forming takes place in a different region of the $\varepsilon_{eq} - \bar{\eta}$ diagram regarding the one where Nakazima tests evolve. As a results, this fact point out that the conventional FFL curve obtained from Nakazima tests translated to the $\varepsilon_{eq} - \bar{\eta}$ field does not allow the failure to be fully assessed in the flanging process by SPIF, as traditionally is intended in the principal strain space. Consequently, to carry out a prediction of failure by fracture in stretch flanging by SPIF of the AA2024-T3 sheet, another approach should be adopted.

A simplistic but effective approach adopted by the authors consists in using iso-damage curves based on the McClintock (1968) interpretation by Atkins (1996). The utility of an iso-damage curve is to illustrate a possible limit within the range of stress triaxiality attained consistent with the McClintock criterion adopted. These iso-damage curve would follow the expression $\varepsilon_{eq} \cdot \bar{\eta} = k$, where 'k' is a calculated constant value.

Figure 13 depicts in black dotted lines the corresponding iso-damaged curves for fracture. The critical value $k = 0.145$ is considered a material constant and it is estimated as the average value for the failed experiment evaluated at the fracture point. Assuming this "iso-damage approach", it is clearly observed both in Figure 13a and Figure 13b that the level of accumulated damage corresponding to the failed experiments (red lines in Figure 13) is higher than the final accumulated damage corresponding to the cases of no failure (blue lines in Figure 13). This fact evidences that the value of equivalent strain is not suitable by itself to predict the fracture. Finally, it is worth mentioning that the lower levels of strains attained for the case of $R_{die} = 20$ compared to $R_{die} = 45$ could be explained from the fact that, in the latter case, the initial length of the specimen is sensibly larger, making the tool to induce longer and intensive straining in the flange.

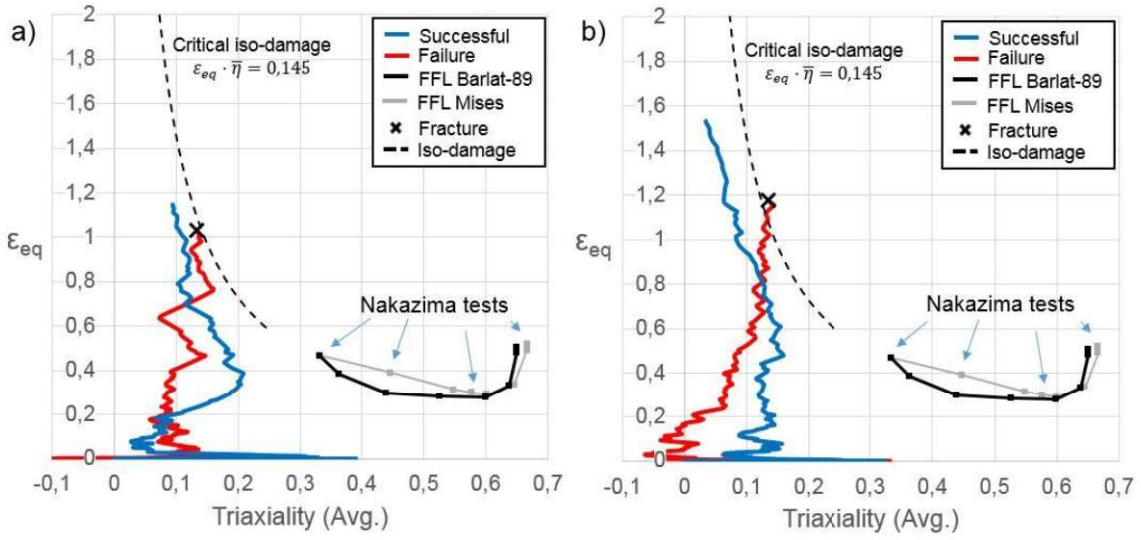

Figure 13. Triaxiality space analysis: Evolution along the flanging process of equivalent strain versus average stress triaxiality for the case of (a) $R_{die} = 20$ mm, initial flange length $l_0 = 15$ mm and initial widths $w_0 = 32$ mm and $w_0 = 36$ mm, and for the case of (b) $R_{die} = 45$ mm, initial width $w_0 = 72$ mm and initial flange lengths $l_0 = 20$ mm and $l_0 = 25$ mm, respectively.

6. Conclusions

This paper presents a systematic study with the aim of analysing the overall flangeability and failure of AA2024-T3 sheet stretch flanged using SPIF. Two typical flange radii in the range of small ($R_{die} = 20$ mm) and medium ($R_{die} = 45$ mm) size were selected. A wide range of parameters was considered including flange widths and lengths, spindle speeds, tool radii and step downs, in order to carry out an intensive experimental campaign for analysing the strain states on the final flanges using CGA.

First of all, a large experimental campaign of stretch flanging by SPIF was performed by considering a wide range of the process parameters with the aim of providing the overall process window. The influence of these parameters in the material formability and failure was evaluated and discussed. In addition, the different modes of failure accomplished were captured and placed within the process window, including beyond the safe zone failure either by fracture at the edge F(E) or fracture at the sheet corner F(C).

In addition, a numerical modelling of the stretch-flanging process was also carried out and, allowing an improved understanding of the process conditions that either allow the manufacturing of the stretch flange or lead to fracture. The numerical results allowed, under the assumption of an analytical framework based on Barlat-89 plasticity criterion (Barlat-89), carrying out the transformation of the material forming limits and the process loading paths from the space of principal strains into the equivalent strain versus stress triaxiality space. This analysis allowed the authors to establish a novel approach based on iso-damage fracture curves for assessing the formability of the stretch-flanging by SPIF.

To sum up, the main contributions of this research work can be summarized as follows:

- Overall experimental definition of the process windows for the stretch flanging process by SPIF, including the assessment of formability and failure within a high range of the most relevant process parameters and the establishment of the safe process zones and main modes of failure for the two radii and material analysed.
- Evaluation of formability and failure within the material FLD for the intrinsically low ductility aluminium alloy AA2024-T3 sheet, which in stretch flanging by SPIF fails uniquely by ductile fracture in mode I of fracture mechanics.
- Development for the first time ever of the analytical framework based on Barlat-89 anisotropy for the transformation of stress/strain states from the principal strain space into the equivalent strain versus stress triaxiality space.
- Explanation of the causes that might influence the enhancement of formability in stretch flanging by SPIF above the conventional (Nakazima) forming limits by using the triaxiality approach exposed.
- Proposition of a new approach for calibrating the prediction of failure in stretch flanging by SPIF based on iso-damage curves derived from the Atkins interpretation of McClintock damage model.

Finally, in the author´s view, further research could be carried out in order to extend these preliminary iso-damage approach to more realistic models including all the stages of ductile fracture, i.e. void initiation, growth and coalescence.

Acknowledgments

The authors wish to thank the Spanish Government for its financial support through the research projects DPI2015-64047-R and PGC2018-095508-B-I00.

References

[1] Allwood JM, Shouler DR. "Generalised forming limit diagrams showing increased forming limits with non-planar stress states", International Journal of Plasticity 2009 Vol. 25, pp. 1207-1230.

[2] ANSYS/LS-DYNA V19.1 User's Guide & Documentation.

[3] ASTM Standard E 517 – 00. Standard method for plastic strain ratio r for sheet metal, 2000.

[4] ASTM Standard E8/E8M – 09. Standard tests methods for tension testing of metallic materials, 2009.

[5] Atkins AG. "Fracture in forming". Journal of Materials Processing Technology 1996; Vol. 56, pp. 609-618.

[6] Bagudanch I, Centeno G, Garcia-Romeu ML, Vallellano C. "Revisiting formability and failure of polymeric sheets deformed by Single Point Incremental Forming". Polymer. Degradation and Stability. 2017, Vol. 144, pp. 366-377.

[7] Bao Y, Wierzbicki T. "On fracture locus in the equivalent strain and stress triaxiality space", International Journal of Mechanical Sciences 2004, Vol. 46(1), pp. 81-98.

[8] Barlat F, Lian J. "Plastic Behaviour and Stretchability of Sheet Metals. Part I: A Yield Function for Orthotropic Sheets Under Plane Stress Conditions". International Journal of Plasticity 1989, Vol. 5, pp. 51-66.

[9] Behera AK, Alves de Sousa R, Ingarao G, Oleksik V. "Single point incremental forming: An assessment of the progress and technology trends from 2005 to 2015". Journal of Manufacturing Processes 2017. Vol. 27, pp. 37-62.

[10] Borrego M, Morales-Palma D, Martínez-Donaire AJ, Centeno G, Vallellano C. "Experimental study of hole-flanging by single-stage incremental sheet forming", Journal of Material Processing Technology 2016, Vol. 237, pp. 320-330.

[11] Centeno G, Bagudanch I, Martínez-Donaire AJ, Garcia-Romeu ML, Vallellano C. "Critical analysis of necking and fracture limit strains and forming forces in single-point incremental forming". Materials & Design 2014, Vol. 63, pp. 20-29.

[12] Centeno G, Martínez-Donaire AJ, Bagudanch I, Morales-Palma D, Garcia-Romeu ML, Vallellano C. "Revisiting formability and failure of AISI304 sheets in SPIF: Experimental approach and numerical validation", Metals 2017. Vol 7(12), pp. 531.

[13] Centeno G, Silva MB, Cristino VAM, Vallellano C, Martins PAF. "Hole-flanging by incremental sheet forming". Journal of Materials Processing Technology 2020. *(In press)*

[14] Cristino VAM, Magrinho JP, Centeno G, Silva MB, Martins PAF. "Theory of single point incremental forming of tubes". International Journal of Machine Tools and Manufacture 2012. Vol. 59, pp. 46-54.

[15] Cui Z, Gao L. "Studies on hole-flanging process using multistage incremental forming", CIRP Journal of Manufacturing Science and Technology 2010, Vol. 2, pp. 124-128.

[16] Duflou JR, Habraken AM, Cao J, Malhotra R, Bambach M, Adams D, Vanhove H, Mohammadi A, Jeswiet J. "Single point incremental forming: state-of-the-art and prospects". International Journal of Material Forming 2017. Vol. 11(6), pp. 743-773.

[17] Emmens WC, Van den Boogaard AH. “An overview of stabilizing deformation mechanisms in incremental sheet forming”. Journal of Material Processing Technology 2009. Vol. 209, pp. 3688-3695.

[18] Emmens WC, Van den Boogaard AH. “The technology of incremental sheet forming - A brief review of the history”. Journal of Materials Processing Technology 2010. Vol. 210, pp. 981-997.

[19] Gatea S, Ou H, McCartney G. “Review on the influence of process parameters in incremental sheet forming”. The International Journal of Advanced Manufacturing Technology 2016. Vol 87(1-4), pp. 479-499.

[20] International Standard ISO 12004-2:2008. Metallic materials-sheet and strip determination of forming limit curves, Part 2: Determination of forming limit curves in the laboratory, 2008.

[21] Iseki H, Kumon H. “Forming limit of incremental sheet metal stretch forming using spherical rollers”. Journal of the Japan Society for Technology of Plasticity 1994. Vol. 35-406., pp. 1336-1341.

[22] Isik K, Silva MB, Tekkaya AE, Martins PAF. “Formability limits by fracture in sheet metal forming”, Journal of Materials Processing Technology 2014, Vol. 214(8), pp. 1557-1565.

[23] Jackson K, Allwood JM. “The mechanics of incremental sheet forming”. Journal of Material Processing Technology 2009, Vol. 29, pp. 1158-1174.

[24] Kitazawa K, Wakabayashi A, Murata K, Seino J. “A CNC incremental sheet metal forming method for producing the shell components having sharp corners”. Journal of the Japan Society for Technology of Plasticity 1994. Vol. 35-406, pp. 1348-1353.

[25] López-Fernández JA, Centeno G, Martínez-Donaire AJ, Morales-Palma D, Vallellano C "Critical evaluation of the formability of AA2024-T3 sheet deformed by single-point incremental forming", DYNA 2019, Vol. 94(5), pp. 523-529.

[26] Magrinho JP, Centeno G, Silva MB, Vallellano C, Martins PAF. "On the formability limits of thin-walled tube inversion using different die fillet radii". Thin-Walled Structures 2019a, Vol. 144, pp. 106328.

[27] Magrinho JP, Silva MB, Centeno G, Moedas F, Vallellano C, Martins PAF. "On the determination of forming limits in thin-walled tubes". International Journal of Mechanical Sciences 2019b, Vol. 155, pp. 381-391.

[28] Martínez-Donaire AJ, Borrego M, Morales-Palma D, Centeno G, Vallellano C. "Analysis of the influence of stress triaxiality on formability of hole-flanging by single-stage SPIF", International Journal of Mechanical Sciences 2019, Vol. 151, pp. 76-84.

[29] Martínez-Donaire AJ, García-Lomas FJ, Vallellano C. New approaches to detect the onset of localised necking in sheets under through-thickness strain gradients, Materials and Design 2014; 57: 135-145.

[30] Martins PAF, Bay N, Skjoedt M, Silva MB. "Theory of single point incremental forming", CIRP Annals - Manufacturing Technology 2008, Vol. 57, pp. 247-252.

[31] Martins PAF, Bay N, Tekkaya AE, Atkins AG. "Characterization of fracture loci in metal forming". International Journal of Mechanical Sciences 2014, Vol. 83, pp. 112-123.

[32] Mason B. "Sheet Metal Forming for Small Batches". Bachelor's Thesis, University of Nottingham, UK, 1978.

[33] McAnulty T, Jeswiet J, Doolan M. "Formability in single point incremental forming: A comparative analysis of the state of the art". CIRP Journal of Manufacturing Science and Technology 2017. Vol. 16, pp. 43-54.

[34] McClintock FA. "A criterion for ductile fracture by the growth of holes". Journal of Applied Mechanics - Transactions ASME 1968, Vol 35, pp. 363-371.

[35] Mirnia MJ, Shamsari M. "Numerical prediction of failure in single point incremental forming using a phenomenological ductile fracture criterion", Journal of Materials Processing Technology 2017, Vol. 244(8), pp. 17-43.

[36] Powel NN, Andrew C. "Incremental forming of flanged sheet metal components without dedicated dies". Proceedings of the Institution of Mechanical Engineers, Part B: Journal of Engineering Manufacture 1992. Vol. 206(1), pp. 41-47.

[37] Silva MB, Nielsen PS, Bay N, Martins PAF. "Failure mechanisms in single-point incremental forming of metals", International Journal of Advanced Manufacturing Technology 2011, 56(9-12), pp. 893-903.

[38] Silva MB, Skjoedt M, Martins PAF, Bay N. "Revisiting the fundamentals of single point incremental forming by means of membrane analysis", International Journal of Machine Tools and Manufacture 2008, Vol. 48(1), pp. 73-83.

[39] Soeiro JMC, Silva CMA, Silva MB, Martins PAF. "Revisiting the formability limits by fracture in sheet metal forming". Journal of Material Processing Technology 2015, Vol. 217, pp. 184-192.

[40] Vallellano C, Morales D, Lomas-Jung FJ "A study to predict failure in biaxially stretched sheets of aluminum alloy 2024-T3", Materials and Manufacturing Processes 2008, Vol. 23(3), pp. 303-310.

[41] Voswinckel H, Bambach M, Hirt G. “Process limits of stretch and shrink flanging by incremental sheet metal forming”. Key Engineering Materials 2013. Vol. 549, pp. 45–52

[42] Voswinckel H, Bambach M, Hirt G. Improving geometrical accuracy for flanging by incremental sheet metal forming. International Journal of Material Forming 2015. Vol. 8(5), pp 391-399.

[43] Vujovic V, Shabaik AH. “A New Workability Criterium for Ductile Metals”, Journals of Engineering Materials and Technology 1986, Vol. 108, pp. 245-249.

[44] Wierzbicki T, Bao Y, Lee Y-W, Bai Y. “Calibration and evaluation of seven fracture models”, International Journal of Mechanical Sciences 2005, Vol. 47, pp. 719-743.